Simultaneously Utilizing Excited Holes and Electrons for Piezoelectric-Enhanced Photoproduction of H_2O_2 from S-Scheme 2D S-doped VO_x/g-C_3N_4 Nanostructures

Huynh Phuoc Toan[1,2], Duc-Viet Nguyen[3], Pham Duc Minh Phan[1,2], Nguyen Hoai Anh[1,2], Pho Phuong Ly[1,2], Minh-Thuan Pham[4,5], Seung Hyun Hur[3], Thuy Dieu Thi Ung[6], Do Danh Bich[7], Hoai-Thanh Vuong[8,*]

[1]Faculty of Chemical Engineering, Ho Chi Minh City University of Technology (HCMUT), 268 Ly Thuong Kiet, District 10, Ho Chi Minh City, Vietnam

[2]Vietnam National University Ho Chi Minh City (VNU-HCM), Linh Trung Ward, Thu Duc City, Ho Chi Minh City, Vietnam

[3]School of Chemical Engineering, University of Ulsan, Ulsan, South Korea

[4]Center for Environmental Toxin and Emerging-Contaminant Research, Cheng Shiu University, Kaohsiung 83347, Taiwan

[5]Institute of Environmental Toxin and Emerging-Contaminant, Cheng Shiu University, Kaohsiung 833301, Taiwan

[6]Institute of Material Science, Vietnam Academy of Science and Technology, Hanoi, Vietnam

[7]Department of Physics, Hanoi National University of Education, 136 Xuan Thuy, Ha Noi, Vietnam

[8]Department of Chemistry and Biochemistry, University of California Santa Barbara (UCSB), Santa Barbara, California 93106, USA

*Corresponding author's contact: hoai-thanh@ucsb.edu

Abstract

The simultaneous use of excited holes and electrons in photocatalytic research has become a strong driving force for rationalizing materials in design and development. As a promising strategy, step-scheme (S-scheme) photocatalysts have enormously ignited the photocatalytic community in recent decades. Introducing piezoelectric fields under light irradiations to generate valuable chemical products, such as hydrogen peroxide (H_2O_2), has also gained current interest in enhancing the large-scale production of these chemicals. In the research, we reported the fabrication of 2D S-doped VO_x deposited on 2D g-C_3N_4 to produce H_2O_2 via the piezo-photocatalytic process. The finding pointed out that adding sulfur to VO_x can help improve the catalytic outcomes by modifying the electronic and morphological properties of pristine VO_x. In addition, when coupled with g-C_3N_4, the presence of sulfur limits the formation of graphene in the VO_x/g-C_3N_4 composites, causing shielding effects in the materials. Besides, the research also sheds light on the charge transportation between g-C_3N_4 and S-VO_x under irradiation and how the composites work to trigger the formation of H_2O_2. It turned out that the formation of H_2O_2 significantly relies on the reduction of oxygen to generate oxygenic radical species at g-C_3N_4 sites. Meanwhile, S-VO_x provides oxidative sites in the composites to oxidize water molecules to generate H_2O_2. This study confirms the validation of S-scheme piezo-photocatalysts, thus encouraging further research on developing heterojunction materials with high catalytic efficiency, which can be used in practical conditions.

Keywords: Vanadium oxides (VO_x), g-C_3N_4, S-scheme charge transfer, H_2O_2 production, piezo-photocatalysis

1. Introduction

Sustainable hydrogen peroxide (H_2O_2) production is fascinating since H_2O_2 finds its essential role in various fields, ranging from water treatment to fuel cells [1, 2, 3]. It has been

predicted that the global demand for H_2O_2 by 2030 will be US$ 15.4 billion, increasing from US$ 10.4 billion in 2022 [4]. However, over 95 % of the current supply has come from the traditional manufacturing of anthraquinone oxidation (AQ), posing some associated demerits of environmental deterioration and intensive cost and energy consumption [5]. Thereby, there is an urgent need to produce this chemical from alternative methods in which solar-to-H_2O_2 conversion offers the potential avenue to realize the expectations.

With inspiration from natural photosynthesis, artificial photosynthesis has been waking up for decades since the splitting of water under UV irradiation on a titanium dioxide (TiO_2) electrode was published [6]. Various semiconductors, such as ZnO, WO_3, and so forth, have been reported to potentially be used as photocatalysts. Multivalent vanadium oxides (VO_x) would be regarded as a competitive candidate. However, the photoactivity from VO_x is relatively unsatisfactory due to the sluggish charge carrier separation [7]. Thus, coupling VO_x with other materials might become a reasonable approach to accelerate the catalytic performance of this exciting oxide. Earliest reports have revealed the catalytic enhancement when uniting VO_x with other oxides, such as TiO_2, ZnO, or SnO_2 [8, 9, 10]. In addition to other metal oxides, coupling VO_x with carbon-based photocatalysts, such as 2D graphitic carbon nitrides (2D g-C_3N_4), is also recorded in the literature [11]. Thanks to the unique properties of 2D structures, depositing VO_x on 2D g-C_3N_4 has captured scientific interest. For example, 0D V_2O_5 nanoparticles or nanodots on 2D g-C_3N_4 were earliest fabricated by Liu and co-workers to remove rhodamine B and amoxicillin in water [12, 13]. Later, various V_2O_5 morphologies anchored 2D g-C_3N_4 were recorded in the literature, such as nanobelts [14], 1D nanorods [15, 16], nanoribbons [17], and recently 2D nanoflakes [18]. Although VO_x with various dimensions and shapes decorated 2D g-C_3N_4 were reported, there are limited studies on 2D VO_x nanosheets decorated 2D g-C_3N_4 nanosheets for photocatalysis, resulting in a knowledge gap in understanding the unique composites. Thus, synthesizing 2D-2D layer structures of VO_x/g-C_3N_4 would be worth exploring in this regime.

To accurately understand charge transfer in heterojunction photocatalysts, in 2019, step-scheme (S-scheme) photocatalysts were introduced by Yu's group after identifying some problems from traditional type-II or Z-scheme mechanisms [19, 20]. Theoretically, an S-scheme heterojunction catalyst comprises two semiconductors, with one being an oxidative photocatalyst in contrast to the reductive photocatalyst from the remaining part. As a result, to form an S-scheme heterostructure, the composites require two materials with highly oxidative and highly reductive properties from separate sides [21, 22]. Due to the efficacy of S-scheme charge transfer routes in recent years, substantial attention has been drawn to fabricating S-scheme photocatalysts to produce H_2O_2 [23]. Besides that, 2D/2D van der Waals heterostructures are believed to possess some distinct features, including accessibility of active sites and maximum charge separation and transportation at the interfaces due to face-to-face interactions [24]. Understandingly, VO_x and g-C_3N_4 can form the S-scheme heterojunction photocatalysts due to the suitable band edge positions of these materials, in which VO_x plays as an oxidative catalyst, and g-C_3N_4 contributes as a reductive side [11]. Nonetheless, less attention has been paid to this exciting composite, and there is no report on the production of H_2O_2 by using van der Waals S-scheme VO_x/g-C_3N_4 in the literature based on our knowledge. Therefore, establishing van der Waals S-scheme VO_x/g-C_3N_4 for generating H_2O_2 might become meaningful in exploring and realizing the concept of solar-to-H_2O_2 conversion in terms of sustainability.

Although S-scheme heterojunction photocatalysts are more efficient regarding charge separation and transfer behaviors, there is still room for electron-hole pair recombination at the interfaces due to structural defects [25]. However, these defects can be a gift for other electric fields, in which a win-win situation can be achieved to enhance catalytic outcomes. In recent years, external stress induced by ultrasound to promote the piezoelectric effects, which can suppress the charge recombination, on the materials has enormously gained scientific interest [26]. This phenomenon frequently originated from non-centrosymmetric structures of the

materials, in which polarizing materials' surfaces can boost the strength of piezoelectricity [27]. A previous study showed that S-scheme g-C_3N_4/V_2O_5 enhanced the removal of tetracycline under simultaneous irradiation of light and ultrasound [28]. Thus, combining the internal electric field (IEF) from S-scheme heterojunctions with the surface piezoelectric effects prompted by sonication can help overcome the structural defects and reach satisfactory performance. Furthermore, elemental doping can be useful in this regime to polarize VO_x surfaces. For example, Jang and colleagues fabricated 2D sulfur (S) -doped V_2O_5 and observed some unique features in the optical and electrical properties of the materials [29]. Hence, it is intriguing to understand the role of S in 2D S-doped VO_x/g-C_3N_4 van der Waals S-scheme heterojunction piezo-photocatalysts regarding the field of solar H_2O_2.

From the above analyses, we fabricated 2D S-doped VO_x/g-C_3N_4 (S-VOCN) S-scheme heterojunction piezo-photocatalysts for the accelerated generation of H_2O_2. The results showed that S-VOCN exhibits relatively better activity at 20.27 mmol g^{-1} h^{-1} compared to other materials, as demonstrated in Table S1. From the findings, sulfur helps to enhance the formation of porosity on VO_x structures to accelerate catalytic performance and enrich the number of defective sites to boost process efficiency. The characterization results show that the formation of H_2O_2 would rely on the formation of oxygenic radical species and water oxidation. Supported by the highly oxidative holes in S-VO_x sites, water can be directly oxidized to produce H_2O_2 and partially generate singlet oxygen ($^1O_2$), which was later reduced to form H_2O_2. Meanwhile, g-C_3N_4 sites mainly contribute to the production of H_2O_2 based on oxygen reduction pathways. These simultaneous reactions can enhance catalytic outcomes, which would strongly validate the usefulness of S-scheme charge transfer and encourage the growth of materials design and development.

2. Catalyst Preparation

The S-VO_x/g-C_3N_4 composites, denoted as S-VOCN, were prepared via a simple one-step calcination process, which involved grinding 10 g of thiourea, 2 g of sulfur, and 9 mmol of ammonium metavanadate (NH_4VO_3). The mixtures were placed in a crucible wrapped with aluminum foil and calcinated at 550 ^oC for 4 hours in the presence of air. After cooling to room temperature, the synthesized products were ground, washed, and stored for further use. For comparison, pure g-C_3N_4 (CN), VO_x, VOCN, and S-VO_x were synthesized via the identical procedure without adding sulfur and V^{5+} for CN, or thiourea for S-VO_x, or sulfur for VOCN, and sulfur and thiourea for VO_x.

3. Results and discussion

3.1 Morphological, Chemical, and Physical Properties

Fig. 1a illustrates the synthetic scheme of S-VO_x/g-C_3N_4 composites by the one-step calcination method. The morphologies of all samples characterized by scanning electron microscopy (SEM) and transmission electron microscopy (TEM) are exhibited in Fig. S1**.** The results show that all samples appear to have sheet-like structures with some differences. Regarding VO_x and VOCN, the sheets are perfectly pristine with no evidence of damage. However, the introduction of sulfur in the synthesis led to the formation of many fragments in the S-VOCN samples. It can be hypothesized that sulfur tends to be oxidized by oxygen to become SO_x and evaporate during the calcination, causing fragments in the final catalytic structures. Furthermore, the morphologies of the VOCN and S-VOCN samples are analyzed by high-resolution TEM and shown in Fig. 1b. It is easy to see that without the addition of sulfur, the sheets of VO_x on CN are intact and long, which is consistent with the TEM results. In contrast, the S-VO_x sheets on CN are dimensionless. The HRTEM images did not show any lattice spacing of both samples, indicating that the composites tend to be more amorphous rather than crystalline structures.

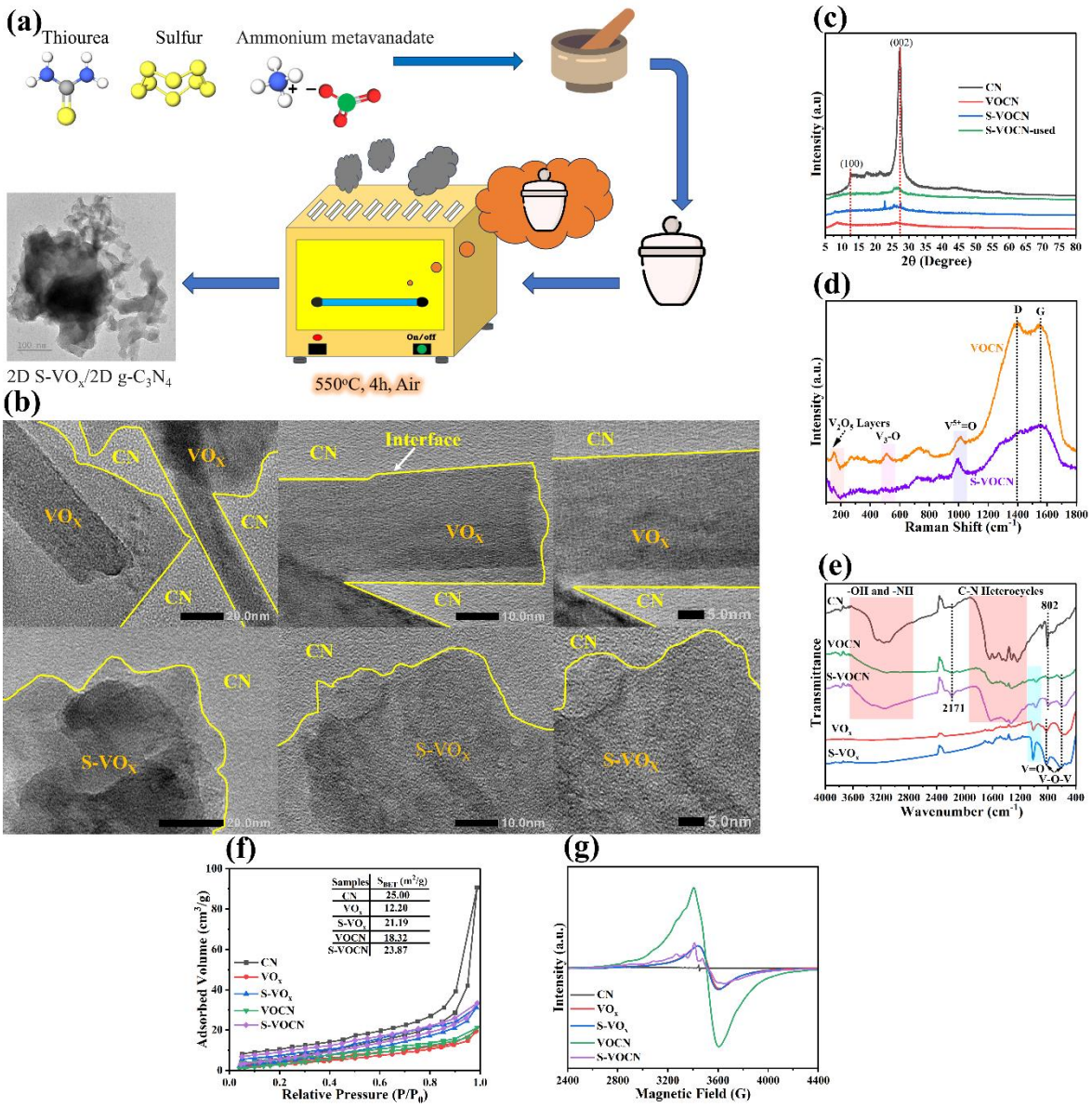

Fig. 1. Schematic Preparation of S-VO_x/g-C_3N_4 (a); HRTEM images of VOCN (above) and S-VOCN (below) (b); XRD patterns of CN, VOCN, S-VOCN, and S-VOCN after four-cycle irradiation (c); Raman spectra of VOCN and S-VOCN (d); FTIR spectra of the as-prepared samples (e); N_2 adsorption-desorption isotherms of CN, VO_x, S-VO_x, VOCN, and S-VOCN (f); solid-state EPR spectra of CN, VO_x, S-VO_x, VOCN, and S-VOCN (g)

To further probe the evidence from the TEM results, the crystallinity of the as-prepared catalysts was characterized by X-ray diffraction (XRD), and the XRD patterns of CN, VOCN, S-VOCN, and S-VOCN after catalysis are presented in Fig. 1b. The XRD patterns of VO_x and

S-VO_x are included in Fig. S2a. The as-prepared oxides exhibit the presence of V_2O_5 and V_6O_{11} in the material's structures. Based on the XRD evidence, while VO_x tends to be more crystalline, S-VO_x has contradicting features with a more amorphous phase in its structures. These proofs indicate the roles of sulfur not only in inducing more porous structures but also in impeding the growth of crystal planes in the synthesized catalysts. For the CN pattern, it is evident that the materials exhibit two distinct features of graphitic structures with two diffraction peaks for (100) and (002) planes. The former peak depicts the replication of heptazine units in the g-C_3N_4 structures, while the latter illustrates the layer-layer stacking in the materials [30]. When forming the composites, the materials become amorphous, as demonstrated in the TEM results with the disappearance of all CN peaks. These features recommend that the addition of other components hinder the growth of CN during the calcination period. Due to the less crystallinity inducing the enhancement in non-centrosymmetric structures, the piezo-catalytic properties of the as-prepared materials can improve. In addition, after catalysis, the peak of around 22.8^o of S-VOCN disappeared, recommending changes in the materials' structures under catalytic conditions.

Furthermore, Raman and Fourier-transformed infrared (FTIR) spectroscopies are used to determine the chemical structures of the as-prepared catalysts. Fig. 1d represents the Raman spectra of VOCN and S-VOCN with the presence of the V_2O_5 layer's structures, V_3-O, and V=O. Interestingly, the presence of D and G bands at around 1400 and 1600 cm^{-1} in VOCN validates that the composites contain some graphene-like regions in the materials [31]. The phenomenon is unclear in S-VOCN, suggesting the hindrance of carbon-species growth in the composites. Graphene is believed to act as an electron acceptor [32]. Thus, the excited electrons can be stored under irradiations, avoiding charge recombination and effectively boosting the catalytic activity. In addition, Fig. S2b points out the full Raman spectra of VO_x and S-VO_x with similar peak positions, matching well with the orthorhombic V_2O_5 structures [33].

With regard to the FTIR spectra, CN shows a well-known pattern of g-C_3N_4 with the presence of C-N heterocycles, -OH, and -NH bonds in the spectra [34]. For VO_x and S-VO_x spectra, the regions under 1200 cm^{-1} typically prove the presence of V=O and V-O-V bonds, which are in excellent accordance with the Raman spectra [16]. The spectra of CN, VOCN, and S-VOCN exhibit the presence of cyano groups on the catalyst's structures at 2171 cm^{-1}, which could help to harvest incident photons in visible regions effectively [35]. Compared to CN and VOCN, S-VOCN possesses a clear feature for this functional group. Notably, the formation of the composites limits the numbers of -OH and -NH_x groups on the surface of the catalysts, which would shift the selectivity toward the production of H_2O_2 instead of H_2O in the reactions [36]. Moreover, solid-state ^{13}C nuclear magnetic resonance (NMR) spectroscopy was applied in this work, as presented in **Fig. S3c**. From the results, the addition of other components during calcination hinders the growth of carbon species in the materials, leading to no peaks in the NMR spectra of VOCN and S-VOCN compared to the distinct features of CN. These results meaningfully validate the changes in the catalyst's structures, enhancing polarizations in which the piezo-catalytic activities can be improved.

It is known that surface charge can influence the catalytic outcomes of the catalysts. Thus, the zeta potential measurements were carried out to understand the surface charge of the synthesized materials. As seen in Table S2, all materials exhibit negative potential in pure water, which could favor attracting more protons to accelerate the formation of H_2O_2. From the results, when sulfur was introduced to VO_x, the surface potential dropped from -35.8 to -27.4 eV, recommending the changes in VO_x electronic structures. However, the composites between VO_x and CN exhibit the lowest surface potential value at -12.6 mV compared to -20.2 mV from S-VOCN. The results suggest that VOCN tends to be more challenging in attracting protons to the surface than S-VOCN. In other words, due to the formation of H_2O_2 requiring the continuous supplements of protons, the more negative value of surface potentials would be one of the indicators of higher catalytic activity. However, due to rapid charge recombination,

component catalysts exhibit lower catalytic performance even though these materials possess higher proton adsorption ability.

In order to study the surface area and porosity of the materials, nitrogen adsorption-desorption measurements were conducted. As seen in Fig. 1f, all samples exhibit a type IV isotherm with H3 hysteresis loop according to the Brunauer-Deming-Deming-Teller classification [37]. Based on the BET surface area, CN presents the highest surface area, in contrast to the lowest one from VO_x. When sulfur was added to the calcination, the surface area of S-VO_x increased nearly 1.7 times compared to pure VO_x. Similarly, the surface area of S-VOCN is also higher than that of VOCN. It is believed that more surface area will lead to lower selectivity in the production of H_2O_2 based on g-C_3N_4-based catalysts due to increasing the number of primary amine groups on the surface, limiting the interactions between O_2 and catalysts [36]. This is true in the case of pure CN in the prepared samples. However, with the formation of the composites, the primary amines in the catalysts' structures are removed, as validated by the FTIR spectra, thus eliminating the barriers in reactant-catalyst interactions. In addition, the effective charge transfer in the heterojunction structures leads to enhanced catalytic outcomes. From the data, it is believed that the presence of sulfur induces many defective sites, which can boost the adsorption and activation of O_2 to accelerate the catalytic performance. Additionally, the average pore size of the prepared samples is presented in Table S2. From the data, VO_x shows the smallest pore size value. The pore size increased 10 times in S-VO_x, confirming the role of sulfur in creating porosity in the catalysts' structures. The composites also exhibit high pore size values compared to the pristine CN. Understandably, the in-situ calcination between CN and VO_x precursors produces a large volume of various gases, which will release and etch the final catalysts to induce the porous structures. Regarding VOCN and S-VOCN, these samples present the same phenomenon as VO_x and S-VO_x in which the addition of sulfur enlarges the pore size of the materials. These results are consistent with TEM analyses.

Fig. 1g depicts the room-temperature electron paramagnetic resonance (EPR) spectra of the as-prepared materials under darkness. As can be seen in the figure, CN exhibits feeble EPR signals compared to other samples, illustrating the small numbers of free electrons in CN. The signal tends to overlap regarding VO_x and S-VO_x spectra, suggesting a similar fraction of free electrons in these samples. However, a significant increase in the intensity was observed in VOCN, while the signal became less intense in S-VOCN. It is hypothesized that free electrons would accumulate in VOCN in a large portion due to the presence of graphene-like structures, leading to the enhancement in the EPR spectra. Although more free electrons can be associated with the improvement in catalytic activities, VOCN did not produce the highest catalytic outcomes due to the lack of active sites, as pointed out by BET results with low surface area and higher charge recombination rate, which will be discussed in the next section.

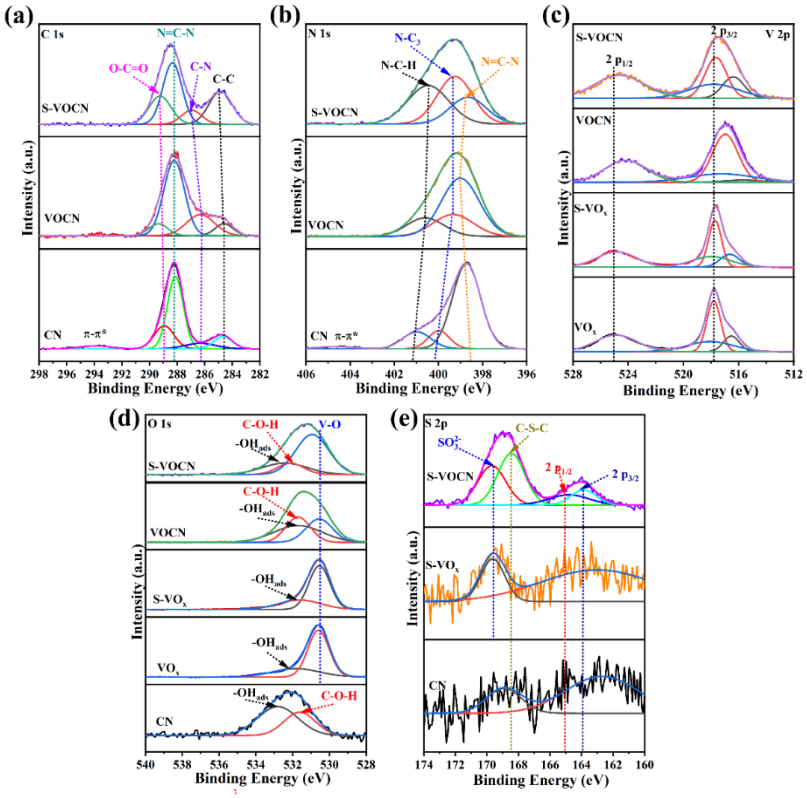

Fig. 2. Core-element XPS spectra of the prepared materials: C 1s (a); N 1s (b); V 2p (c); O 1s (d); S 2p (e)

X-ray photoelectron spectroscopy (XPS) was also performed in this study to understand each element's charge transfer and oxidation states in the synthesized catalysts. Fig. 2a and 2b show the C 1s and N 1s spectra of S-VOCN, VOCN, and CN. All samples contain C-C, C-N, N=C-N, and O-C=O bonds in the C 1s spectra, while N=C-N, N-C_3, and N-C-H bonds are present in the N 1s spectra with minor shifts. The results validate the presence of g-C_3N_4 structures in the synthesized composites. A careful characterization without deconvoluted peaks shows that VOCN and S-VOCN exhibit the peaks at higher binding energy regions, confirming the charge transfer from CN to VOCN or S-VOCN under darkness to balance the Fermi level [37, 38, 39, 40]. Similarly, the V 2p spectra in Fig. 2c show the oxidation state of V at +5 [41]. Between the composites and the pristine samples, the general peaks without deconvolutions appear at lower binding energy regions, pointing out that VOCN and S-VOCN receive electrons to enrich the electron densities in the VO_x sites of the composites. The results would be consistent with the EPR results. Due to oxygen in all samples, the O 1s spectra in Fig. 2d exhibit different charge transfer phenomena compared to V 2p. If oxygen is only present in the oxide phases, the binding energy of the composites would be in the lower regions, as followed by the patterns of V 2p due to the electron density enrichment phenomenon. The observations are in the opposite direction, in which the binding energy peak of the composites is between CN and VO_x or S-VO_x. Thus, using the O 1s spectra to understand the charge transfer phenomenon is hard. Based on this analysis, it can be thought that the spectra of C 1s, N 1s, and V 2p could be reasonably used to estimate the charge transportation under darkness. Finally, Fig. 2e exhibits the presence of S 2p in CN, S-VO_x, and S-VOCN with different S species with the oxidation of +2 in the samples, including SO_3^{2-} and C-S-C [42, 43]. As a result, the evidence from the XPS spectra validates the successful synthesis of the designed composites and the charge transportation under darkness to balance the Fermi level of the composites from CN to VO_x or S-VO_x, which would be related to S-scheme charge transfer mechanisms in the dark.

3.2 Piezo-photocatalytic Performance

The piezo-photocatalytic performance of the as-prepared catalysts toward the production of H_2O_2 was recorded in this work to estimate the catalytic efficacy of the materials. Fig. 3a shows the comparison results between different catalysts comprising CN, VO_x, S-VO_x, VOCN, and S-VOCN. As can be observed from the data, both CN and VO_x exhibit the evolution rate of H_2O_2 at 13.98 and 11.08 mmol g^{-1} h^{-1}, respectively. Adding sulfur helps enhance the catalytic outcomes, with the figure being 14.51 mmol g^{-1} h^{-1} compared to pristine VO_x. It can be inferred that sulfur induced multiple defects in the structures, which can help to effectively trap excited electrons to prevent charge recombination, causing enhancement in the catalytic outcomes. When S-VO_x is coupled with CN to form S-VOCN, the catalytic result significantly increases to 20.27 mmol g^{-1} h^{-1}, owing to multiple surface defects in the structures. However, the composites between VO_x and CN exhibit low catalytic outcomes at just 12.80 mmol g^{-1} h^{-1}, which was higher than that of VOx but lower than CN. This phenomenon can be due to the presence of graphene in the VOCN composites, as demonstrated by the Raman spectra. With the appropriate percentage of graphene, the catalytic outcomes can be enhanced since graphene can act as an electron acceptor. However, with the excess amount of graphene, the composites will turn dark, which could produce the shielding effects to diminish the catalytic outcomes [44]. Adding sulfur reduced the possibility of graphene formation to avoid shielding effects and increased surface defects, acting as active centers to enhance catalytic results. Thus, the results would be understandable, and S-VOCN was selected to proceed with more insightful experiments. Besides that, the stability of S-VOCN is shown in Fig. S3a, where the catalytic performance nearly remained unchanged after four running cycles, suggesting the long-term uses of the as-prepared catalysts.

Furthermore, piezo-catalytic, photocatalytic, and piezo-photocatalytic experiments based on S-VOCN were conducted to evaluate the effectiveness of the piezo-photocatalytic process. In Fig. 3b, the results show the comparison data between photocatalytic, piezo-catalytic, and piezo-photocatalytic processes. In particular, if the system only shines with light,

the generation of H_2O_2 was at 6.06 mmol g^{-1} h^{-1}. Meanwhile, solely sonicating the catalysts in the dark can produce 11.48 mmol g^{-1} h^{-1} of H_2O_2. The results are consistent with previous records [30, 45]. This is because of the significant differences between ultrasonic and light intensity. In addition, the absorption of incoming photons from the materials is favored at specific wavelengths, and incident photons come from just one direction, which can limit the catalytic outcomes. In contrast, the absorption of vibration energy from the materials is more efficient since ultrasound spreads from all directions of the reactors, leading to better results in the piezo-catalytic process. Moreover, combining light and ultrasound can increase the yield of H_2O_2 up to 20.48 mmol g^{-1} h^{-1}, nearly 3.3 and 1.77 times when compared with only light or ultrasound, respectively, proving the existence of synergistic effects between light and ultrasound during the catalytic process.

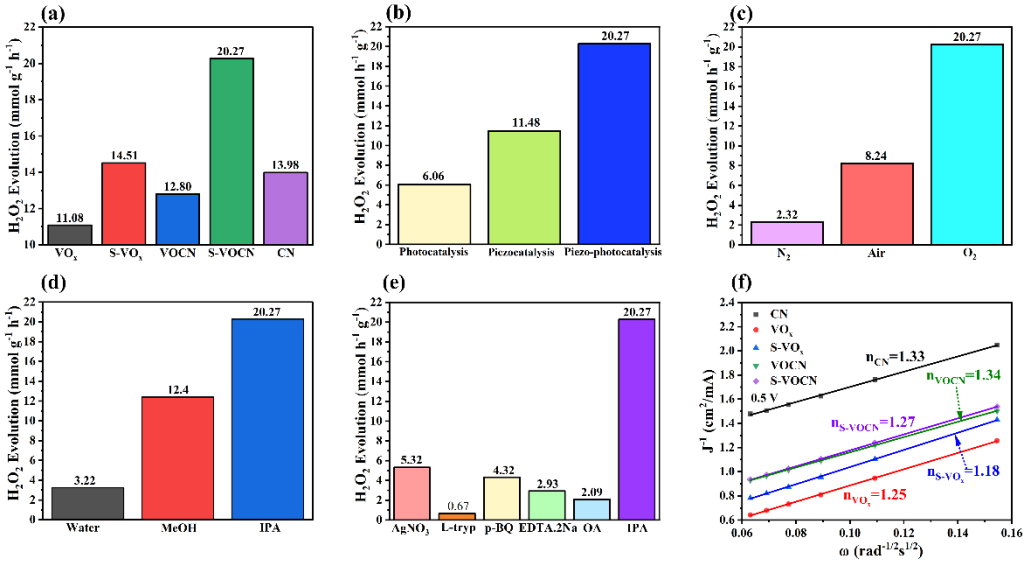

Fig. 3. Piezo-photocatalytic performance of CN, VO_x, S-VO_x, VOCN, and S-VOCN (a); Photocatalysis, piezo-catalysis, and piezo-photocatalysis of H_2O_2 production from S-VOCN (b); Piezo-photocatalysis of H_2O_2 from S-VOCN under different gas conditions (c); Piezo-photocatalysis of H_2O_2 from S-VOCN from using different sacrificial agents (d); Piezo-photocatalytic generation of H_2O_2 from S-VOCN with using different scavengers (e); Koutecky-Levich plots of CN, VO_x, S-VO_x, VOCN, and S-VOCN (f)

Undoubtedly, the formation of H_2O_2 is mainly based on the direct or indirect reduction of O_2 or the oxidation of water [46]. Thus, different gases were used to bubble the solution during the process. Understandably, introducing O_2 in the reaction will favor the generation of H_2O_2, leading to the highest catalytic performance. Expectedly, when N_2 was introduced to the reactor, the lowest catalytic outcome was recorded at 2.32 mmol g^{-1} h^{-1}. It can be suggested that the formation of H_2O_2 in the inert atmosphere can originate from water oxidation instead of oxygen reduction pathways. The possible mechanism will be discussed in detail in the next section. Moreover, for industrialization purposes, it is more likely to generate H_2O_2 under ambient conditions to reduce manufacturing costs rather than using pure oxygen as a reactant. Therefore, the reaction was also run under air conditions, with the generation rate of H_2O_2 being recorded at 8.24 mmol g^{-1} h^{-1}. Although the catalytic performance under air conditions was lower than under oxygen, this can be a good sign for validating the potential of generating H_2O_2 by piezo-photocatalysis under air conditions, which can help diminish the cost and obtain the target of on-site H_2O_2.

Comprehensively, the presence of sacrificial agents would influence the production of H_2O_2 due to the hole-scavenging properties to avoid charge recombination. Thus, the control experiments with and without using a sacrificial agent were undertaken. As can be seen in Fig. 3d, the use of pure water would anticipatedly produce a limited quantity of H_2O_2, with the data being 3.22 mmol g^{-1} h^{-1}, while the catalytic outcome increases nearly 3.9 and 6.3 times when adding methanol (MeOH) or isopropanol (IPA) in the reaction. It is because excited holes were consumed by these agents to prevent electron-hole pair recombination, accelerating the production yield.

Further radical trapping experiments were conducted to study the roles of radicals in generating H_2O_2. Notably, silver nitrate ($AgNO_3$), L-tryptophan (L-tryp), and para-benzoquinone (p-BQ) were added to the solution to scavenge excited electrons (e^-), $^1O_2$, and

superoxide ($^{-}O_2^{\cdot}$), respectively [47]. The catalytic performance in Fig. 3e exhibits the strong dependence of H_2O_2 on forming oxygenic radicals, indicating that the catalytic mechanism entails the radical pathways from the reduction and oxidation of oxygen species. There is no doubt that $AgNO_3$ will compete with O_2 to consume excited electrons, and the production of H_2O_2 was limited due to the unavailability of electrons to reduce oxygen. However, the catalytic outcomes seriously decreased when oxygen species radicals were trapped, as presented in the case of trapping superoxide and $^1O_2$.

Further proof from the nitrotetrazolium blue chloride (NBT) degradation Fig. S3b certifies the continuous superoxide formation in the solution because NBT was known to react with superoxide to produce monoformazan [48]. It is understandable that in the case of pure water, the produced concentration of superoxide was low, leading to the low degradation yield of NBT. However, when IPA was added, the amount of $^{-}O_2^{\cdot}$ enormously increased over time due to the effectiveness of avoiding charge recombination, resulting in a high NBT degradation rate. Interestingly, when L-tryp was added with NBT in the reaction, the degradation performance of NBT reduced, recommending the competition of excited holes and NBT to react with $^{-}O_2^{\cdot}$ to produce $^1O_2$ or monoformazan, sequentially. In the case of trapping excited holes (h^+), ethylenediaminetetraacetic acid disodium (EDTA-2Na) and oxalic acid (OA) were used. Consequently, the excited hole scavenging evidence shows that the water oxidation partially takes part in producing H_2O_2. These fascinating results give insight into the catalytic mechanisms involving water oxidation and oxygenic radical pathways and the charge transfer mechanism in the heterojunction catalysts, associating with S-scheme charge transfers, which will be fully explained in the next section.

Eventually, the work employed electrocatalytic techniques, including linear sweep voltammetry (LSV) and cyclic voltammetry (CV), by using a rotating disk electrode (RDE) to validate the findings from piezo-photocatalytic experiments. All samples exhibit the reduction

ability toward oxygen from CV measurements, as presented in Fig. S4, with the reduction peak being around 0.5 V vs. RHE. Additionally, the LSV measurements of all samples in Fig. S5 show an increase in the reduction when the rotating speeds accelerate. These results validate the ability to reduce oxygen to produce water or H_2O_2. From the LSV data, the number (n) of electron transfers is calculated and shown in Fig. 3f, where all samples depict the n values that are higher than 1 and lower than 2, suggesting the reduction toward the formation of H_2O_2 from oxygen via single-electron and dual-electron transfers. The data is consistent with the results from the piezo-photocatalytic performance, where the way to generate H_2O_2 is mainly from oxygenic radical species.

3.3 Optical and Charge Transfer Behaviors

Optical properties are one of the essential factors for obtaining insights into photocatalytic studies. Thus, to understand this contributing factor, Ultraviolet diffuse reflectance spectroscopy (UV-DRS) was employed. Fig. 4a presents the UV-DRS spectra of all samples, in which the characteristics of CN are consistent with the literature [49]. It is easy to see that VO_x illustrates the broad spectra in the UV-DRS measurements, while S-VO_x exhibits more apparent peaks in the UV and visible regions. Understandably, the absorption peak is not as strong due to multi-oxidation states in VO_x, which used to be observed in the preliminary publication [50]. A similar phenomenon was observed in the case of VOCN and S-VOCN. However, the absorbance increases in both cases, indicating that the formation of heterojunction photocatalysts effectively boosts the light absorption capacity, potentially correlated to the enhanced catalytic outcomes.

Furthermore, the bandgap energy of CN, VO_x, and s-VO_x was exported based on a Kubelka-Munk model, and the results are illustrated in Fig. 4b. The exported bandgap energy of VO_x and CN are 1.70 and 2.64 eV, respectively, which is in good agreement with the published value [51, 52]. The addition of sulfur modifies the optical properties of VO_x, leading to the increase in the bandgap energy to 2.27 eV, which can significantly contribute to the

catalytic performance due to the shift in the conduction band (CB) or valance band (VB) of the materials, which will clarify in the catalytic mechanism section. The midgap energy is also observed in the CN sample, owing to the presence of defective states in the materials, which is believed to accelerate the catalytic outcomes by reducing the needed incident photon energy to excite the catalysts [53, 54]. These results further confirm the roles of sulfur in modifying VO_x electronic structures to enhance catalytic outcomes of a single component and a composite of VO_x and CN.

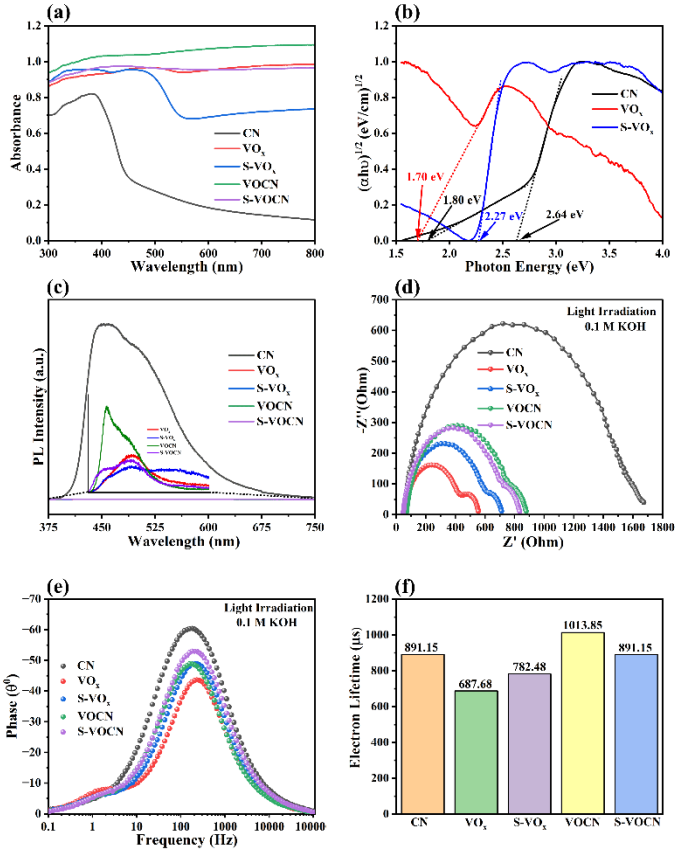

Fig. 4. UV-DRS spectra of the prepared catalysts (a); Optical bandgap energy of the materials exported from a Kubelka-Munk model (b); Photoluminescence (PL) spectra of CN, VO_x, S-VO_x, VOCN, and S-VOCN (c); Electrochemical impedance spectroscopy (EIS) of the synthesized materials under light irradiation (d); Bode-phase plots of the EIS spectra of the as-prepared samples (e); and Photoelectron lifetime of all samples exported from Bode-phase plot results (f)

Photoluminescence (PL) spectroscopy was recruited in this research to understand the charge recombination properties of the materials. As presented in Fig. 4c, CN shows the most significant intensity with the peak centering around 460 nm compared to other samples, indicating that the charge recombination rate in this sample is serious, corresponding to its low catalytic activity. On the contradictory side, VO_x, S-VO_x, and two composites exhibit low intensity with the intensity following VOCN > VO_x > S-VOCN > S-VO_x. This result illustrates two convincing conclusions. First, constructing the composites between CN and metal oxides circumvents charge recombination. Secondly, doping sulfur to VO_x and VOCN can help reduce the materials' charge recombination rate, certifying better catalytic results. In addition, PL spectroscopy is also a beautiful technique for understanding defect states in the materials [55]. Hence, the results demonstrate that S-VO_x presents more defective states on the surface to quench the photoluminescence properties.

To confirm the PL results, EIS techniques were employed in the work, with the results being depicted in Fig. 4d. It is accepted that the higher radius in the EIS result can illustrate the higher resistance, relating to lower charge transfer efficiency in the sample [56]. Thus, based on the results, CN exhibited lower charge transfer efficiency than other samples, which can be in good agreement with the PL measurements. One notable feature is that VO_x presents a lower radius in the Nyquist plot than S-VO_x, while the radius of S-VOCN is slightly lower than that of VOCN. The Nyquist radii of VO_x and S-VO_x illustrate the contrast phenomenon with the PL spectra. It is understandable that when sulfur is added to VO_x, the materials become more defective compared to VO_x. These defective states can act as electron traps on the surface and active sites to accelerate catalytic rates. In the electrocatalytic measurements, these defects can limit the flexibility of electrons, leading to higher resistance, as frequently observed in the literature [57, 58]. Hence, the PL and EIS results confirm the roles of defective states in different measurements, which could impact the specific catalytic processes. Both techniques give the

same conclusion with better catalytic activity when forming heterojunction photocatalysts due to easing serious charge recombination situations.

Furthermore, the Bode-phase plots were exported from EIS measurements to interpret the electron transfer capability and photoelectron lifetimes. As shown in Fig. 4e, the Bode-phase plot of CN exhibits the peak at a low-frequency region compared to that of other samples. In the case of VO_x, a higher frequency was observed. However, when sulfur was doped to VO_x, S-VO_x represents the lower frequency, indicating that sulfur doping modified the photo properties of VO_x, which can help to prolong the charge lifetime. From the Bode-phase plots, the lifetime of photoelectrons can be estimated via the expression (1):

$$\tau = \frac{1}{2\pi f} \tag{1}$$

where f is the frequency and τ is the photoelectron lifetime.

The calculated lifetimes are illustrated in Fig. 4f, in which CN exhibits a lifetime of 891.15 µs, near the reported value [59]. The estimated values for VO_x and S-VO_x are 678.68 and 782.48 µs, which can further validate the role of surface traps in lengthening the longevity of excited electrons to avoid charge recombination. Interestingly, the lifetime of VOCN appears to be the highest value in all samples, with the data being 1013.85 µs, which further indicates the electron acceptance of graphene in VOCN samples, leading to the highest value in the electron lifetime. Although the result turns out that VOCN potentially tends to exhibit the highest generated H_2O_2, the catalytic performance is the opposite way, further certifying the essential role of an appropriate amount of graphene and surface-active sites in the composites to accelerate catalytic outcomes. In addition, S-VOCN has higher surface-active sites with the addition of sulfur. Thus, even if the charge lifetime is not as good as VOCN, the catalytic outcomes are still better. The other observation under light irradiation of these calculated values in two composites shows that excited electrons under light irradiation tend to stay at CN sites

rather than VO_x or S-VO_x or transfer between CN and VO_x or S-VO_x. If some electrons were transported from CN to VO_x or S-VO_x, the values of charge lifetime should be in the middle of two semiconductors. Likewise, if excited electrons in the composites were likely to remain at VO_x or S-VO_x sites, the calculated values should be near these semiconductors. However, the observation is in the opposite direction, indicating that excited electrons would stay in CN sites, which can correlate to the S-scheme charge transfer mechanism under light irradiation.

3.4 Possible Catalytic Mechanisms

From the previous discussion, the possible catalytic mechanisms of the composites may follow two main pathways, including radicals and water oxidation, based on the radical trapping experiment data. XPS-VB spectra were undertaken to elucidate the results further and determine the VB position in the redox scale of the as-prepared materials. As exhibited in Fig. 5a to 5c, the valance band maximum (VBM) of the materials was exported, with the figures being 2.02, 3.07, and 3.15 eV for CN, VO_x, and S-VO_x, respectively. The VB and CB positions and work functions of the materials are exported via Equations (2), (3), and (4) [60, 61, 62].

$$E_{VB} = \Phi + E_{XPS-VB} - 4.44 \quad (2)$$

$$E_{CB} = E_{VB} - E_g \quad (3)$$

$$W = \Delta V + \Phi \quad (4)$$

where E_{VB}, E_{CB}, and E_g are the VB, CB, and bandgap energy (eV), respectively, $E_{XPS\text{-}VB}$ is the VBM exported from XPS-VB, Φ is the working function of the analyzer that is equal to 3.88 eV, W is the work function of the materials, and ΔV is the contact potential difference from XPS-VB.

From the calculations, the VB positions of CN, VO_x, and S-VO_x are 1.46, 2.51, and 2.59 eV, respectively, while the CB positions of these samples are, in turn, -1.18, 0.81, and 0.32 eV. Based on the calculations, the band structure diagram of these samples is exhibited in Fig. 5d.

It is intriguing to observe that adding sulfur would shift the CB position of VO_x to the lower position, with ΔE being nearly 0.5 eV, indicating the increase in reducibility of the S-VO_x sample. The work function of CN, VO_x, and S-VOx are also computed via the distance between two inflection points in the XPS-VB spectra, with the results being 5.59, 6.42, and 6.6 eV. The proofs meaningfully reveal that the charge transfer happens under irradiation of the composites to generate H_2O_2, following strictly S-scheme heterojunction charge transfer mechanisms.

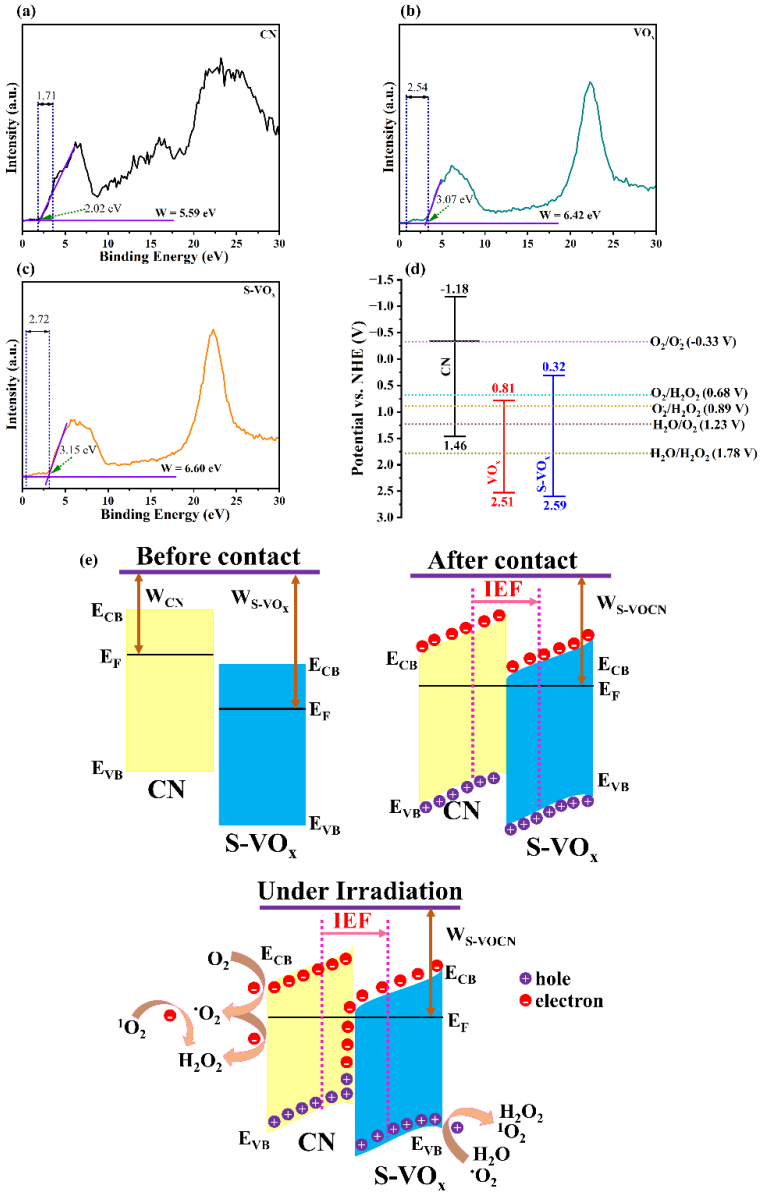

Fig. 5. XPS-VB spectra of CN (a), VO_x (b), and S-VO_x (c); Band structure diagram of CN, VO_x, and S-VO_x (d); and Possible S-scheme charge transfer mechanism (e)

Due to the similarity in charge transfer of VOCN and S-VOCN, the charge transfer mechanism was drawn for only S-VOCN and presented in Fig. 5e. In particular, the Fermi level of two semiconductors, CN and S-VO_x, shows the difference before joining into contact. When two components come into contact, the electrons flow from CN to S-VO_x to balance the Fermi level. Such movements induce the negative and positive charge layers at the interfaces between CN and S-VO_x. The formation of these layers leads to the establishment of an internal electric field (IEF) directing from CN to S-VO_x to guide electrons moving in a specific direction. When reaching equilibrium, upward and downward band bending occurs at CN and S-VO_x sites near the interfaces, respectively, to ensure the stable alignment of the Fermi level in the composites. Under irradiation, the useless electrons from S-VO_x and useless holes from CN tend to recombine at the interface due to coulombic force. Meanwhile, the highly reductive electrons and oxidative holes under excited states will be maintained at the CB of CN and VB of S-VO_x to help proceed with the redox reactions effectively, accelerating the catalytic outcomes [23, 63].

From the above mentions, it is easy to know that the potential to convert O_2 to $^{\cdot}O_2^-$ is nearly -0.33 eV, which, from our result, just CN can have sufficient strength to conduct since VO_x and S-VO_x exhibit the positive CB potential. Based on the trapping experiments, the formation of H_2O_2 strongly relies on the formation of $^{\cdot}O_2^-$, indicating that the reduction of O_2 to superoxide mainly occurs by the accumulation of excited electrons at CN sites. Otherwise, less radical dependence was observed in the research. In addition, the formation of H_2O_2 in the inert environment illustrates the opposite direction of excited holes, in which water molecules were oxidized at VO_x or S-VO_x sites to produce H_2O_2. If excited holes from CN oxidized water molecules, the product would be mainly O_2 since the CB potential of VO_x or S-VO_x can not reduce O_2 to produce superoxide. The direct reduction from O_2 to H_2O_2 can happen in S-VO_x sites due to partially excited electrons. However, this phenomenon is less favorable because the

flow of electrons would thermodynamically recombine with excited holes at the interfaces of heterojunction photocatalysts. Thus, the formation of H_2O_2 in the inert atmosphere would be primarily from the direct oxidation of water at VO_x or S-VO_x sites. Even with the evolution of O_2 from water oxidation at VO_x or S-VO_x sites, the generation of H_2O_2 from these sites is still likely unable to occur at VO_x or S-VO_x sites due to the abovementioned reasons. The reduction of born O_2 can occur at CN sites to generate superoxide before turning into H_2O_2. This situation also points out that CN sites are reductive and VO_x or S-VO_x sites are oxidative, which accords with the S-scheme charge transfer.

$$O_2 \longrightarrow \cdot O_2^- \longrightarrow {}^1O_2 \longrightarrow H_2O_2 \quad (5)$$

$$2H_2O + 2h^+ \rightarrow H_2O_2 + 2H^+ \quad (6)$$

Based on the results, Equations (5) and (6) would summarize the formation of H_2O_2. Briefly, H_2O_2 was generated under irradiation from S-VOCN and VOCN according to S-scheme heterojunction charge transfers, described in the following steps. O_2 was reduced based on excited electrons at CN sites to produce $^{-}O_2^{\cdot}$ prior to reacting with other excited electrons to form H_2O_2. Meanwhile, excited holes from VO_x or S-VO_x partially oxidized $^{-}O_2^{\cdot}$ to generate $^1O_2$, which can be further reduced by excited electrons to manufacture H_2O_2. At the same time, water oxidation potentially occurs at the VO_x or S-VO_x sites to generate H_2O_2 or O_2, which can be reduced at CN sites to produce final products.

4. Conclusion

In synopsis, the research shows the roles of sulfur-doped in VO_x, which can help modify the synthesized materials' electronic and morphological properties. When cooperating with g-C_3N_4, the presence of sulfur in the synthesis prevents the formation of access graphene sites, which would induce shielding effects and reduce catalytic outcomes. The S-scheme charge

transfer heterojunction piezo-photocatalysts based on S-VO_x and g-C_3N_4 turn out with high efficiency and the ease of synthetic method. In this work, the simultaneous use of excited holes and electrons would enhance the catalytic outcomes. At the g-C_3N_4 sites, oxygen reduction to oxygenic radicals is favorable, while water oxidation at S-VO_x sites is the main reason for generating H_2O_2. Our analyses certify the use of S-scheme heterojunctions to take advantage of both excited holes and electrons simultaneously, which can help realize the practical application of photocatalytic research in industrial and real-world contexts. Finally, these results would hope to motivate other scientists to further fabricate materials by taking away toxic agents and multi-step synthesis, which would violate the sustainability goals as well as the reproducibility of catalysts.

Supporting Information

Materials, Characterizations, Experiment Procedures, A summary of catalytic results from the literature and our work, Physical properties of as-prepared materials, TEM and SEM images, XRD patterns, Raman spectra, NMR spectra, Catalytic results, Electrocatalytic results

Acknowledgments

We acknowledge Ho Chi Minh City University of Technology (HCMUT), VNU-HCM, and Prof. Phung K. Le for supporting this study. Hoai-Thanh Vuong thanks the support from the Vingroup Science and Technology Scholarship program and the UCSB Chancellor Fellowship.

Conflict of Interest

The authors declare no conflict of interest.

Data Availability Statement

The data that support the findings of the study are available from the co-responding authors upon the reasonable request.

References

[1] Ksibi M. Chemical oxidation with hydrogen peroxide for domestic wastewater treatment. *Chem. Eng. J.* **2006**, *119*, 161-165. DOI: 10.1016/j.cej.2006.03.022

[2] Mase, K.; Yoneda, M.; Yamada, Y.; Fukuzumi, S. Seawater usable for production and consumption of hydrogen peroxide as a solar fuel. *Nat. Commun.* **2016**, *7*, 11470. DOI: 10.1038/ncomms11470

[3] Vuong, H.-T.; Nguyen, D.-V.; Phuong, L. P.; Minh, P. P. D.; Ho, B. N.; Nguyen, H. A. Nitrogen-rich graphitic carbon nitride (g-C_3N_5): Emerging low-bandgap materials for photocatalysis. *Carbon Neutralization* **2023**,1-33. DOI: 10.1002/cnl2.65

[4] Tan, D.; Zhuang, R.; Chen, R.; Ban, M.; Feng, W.; Xu, F.; Chen, X.; Wang, Q. Covalent Organic Frameworks Enable Sustainable Solar to Hydrogen Peroxide. *Adv. Funct. Mater.* **2023**, 2311655. DOI: 10.1002/adfm.202311655

[5] Hou, H.; Zeng, X.; Zhang, X. Production of Hydrogen Peroxide by Photocatalytic Processes. *Angew. Chem. Int. Ed.*, vol. 59, pp. 17356-17376, 2020. DOI: 10.1002/anie.201911609

[6] Fujishima, A.; Honda, K. Electrochemical Photolysis of Water at a Semiconductor Electrode. *Nature* **1972**, *238*, 37-38. DOI: 10.1038/238037a0

[7] Wang, S.; Li, Z.; Guan, Y.; Lu, L.; Shi, Z.; Weng, P.; Yan, S.; Zou, Z. Visible light driven TaON/V_2O_5 heterojunction photocatalyst for deep elimination of volatile-aromatic compounds. *Appl. Catal. B* **2019**, *245*, 220-226. DOI: 10.1016/j.apcatb.2018.12.067

[8] Martha, S.; Das, D. P.; Biswal, N.; Parida, K. M. Facile synthesis of visible light responsive V_2O_5/N,S–TiO_2 composite photocatalyst: enhanced hydrogen production and phenol degradation. *J. Mater. Chem.* **2012**, *22*, 10695. DOI: 10.1039/C2JM30462G

[9] Yin, H.; Yu, K.; Song, C.; Huang, R.; Zhu, Z. Synthesis of Au-Decorated V_2O_5@ZnO Heteronanostructures and Enhanced Plasmonic Photocatalytic Activity. *ACS Appl. Mater. Interfaces* **2014**, *6*, 14851-14860. DOI: 10.1021/am501549n

[10] Shahid, M.; Shakir, I.; Yang, S.-J.; Kang, D. J. Facile synthesis of core–shell SnO_2/V_2O_5 nanowires and their efficient photocatalytic property. *Mater. Chem. Phys.* **2014**, *124*, 619-622. DOI: 10.1016/j.matchemphys.2010.07.023

[11] Hong, Y.; Jiang, Y.; Li, C.; Fan, W.; Yan, X.; Yan, M.; Shi, W. In-situ synthesis of direct solid-state Z-scheme V_2O_5/g-C_3N_4 heterojunctions with enhanced visible light efficiency in photocatalytic degradation of pollutants. *Appl. Catal. B* **2016**, *180*, 663-673. DOI: 10.1016/j.apcatb.2015.06.057

[12] Liu, Q.; Fan, C.; Tang, H.; Sun, X.; Yang, J.; Cheng, X. One-pot synthesis of g-C_3N_4/V_2O_5 composites for visible-light-driven photocatalytic activity. *Appl. Surf. Sci.* **2015**, *358*, 188-195. DOI: 10.1016/j.apsusc.2015.09.010

[13] Le, S.; Zhu, C.; Cao, Y.; Wang, P.; Liu, Q.; Zhou, H.; Chen, C.; Wang, S.; Duan, X. V_2O_5 nanodot-decorated laminar C_3N_4 for sustainable photodegradation of amoxicillin under solar light. *Appl. Catal. B* **2022**, *303*, 120903. DOI: 10.1016/j.apcatb.2021.120903

[14] Devarayapalli, K.C.; Lee, K.; Do, H.-B.; Dang, N. N.; Yoo, K.; Shim, J.; Vattikuti, S.V. P. Mesostructured g-C_3N_4 nanosheets interconnected with V_2O_5 nanobelts as electrode for coin-cell-type-asymmetric supercapacitor device. *Mater. Today Energy* **2021**, *21*, 100699. DOI: 10.1016/j.mtener.2021.100699

[15] Dadigala, R.; Bandi, R.; Gangapuram, B. R.; Dasari, A.; Belay, H. H.; Guttena, V.; Fabrication of novel 1D/2D V_2O_5/g-C_3N_4 composites as Z-scheme photocatalysts for CR degradation and Cr (VI) reduction under sunlight irradiation. *J. Environ. Chem. Eng.* **2019**, *7*, 102822. DOI: 10.1016/j.jece.2018.102822

[16] Pham, V. V.; Tran, H. H.; Cao, T. M. V_2O_5 Nanorod-Loaded g-C_3N_4 Sheets for Efficient Photocatalytic Removal of NO and Minimal NO_2 Yield under Visible Light. *Energy Fuels* **2023**, *37*, 13241–13249. DOI: 10.1021/acs.energyfuels.3c01422

[17] Hassan, A. E.; Elsayed, M. H.; Hussien, M. S. A.; Mohamed, M. G.; Kuo, S.-W.; Chou, H.-H.; Yahia, I. S.; Mohamed, T. A.; Wen, Z. V_2O_5 nanoribbons/N-deficient g-C_3N_4 heterostructure for enhanced visible-light photocatalytic performance. *Int. J. Hydrog. Energy* **2023**, *48*, 9620-9635. DOI: 10.1016/j.ijhydene.2022.12.009

[18] Bharathi, K.; Sathiyamoorthy, K.; Bakiyaraj, G.; Archana, J.; Navaneethan, M. 2D V_2O_5 nanoflakes on 2D p-gC_3N_4 nanosheets of heterostructure photocatalysts with the enhanced photocatalytic activity of organic pollutants under direct sunlight. *Surf. Interfaces* **2023**, *41*, 103219. DOI: 10.1016/j.surfin.2023.103219

[19] Zhu, B.; Sun, J.; Zhao, Y.; Zhang, L.; Yu, J. Construction of 2D S-Scheme Heterojunction Photocatalyst. *Adv. Mater.* **2023**, 2310600. DOI: 10.1002/adma.202310600

[20] Fu, J.; Xu, Q.; Low, J.; Jiang, C.; Yu, J. Ultrathin 2D/2D WO_3/g-C_3N_4 step-scheme H_2-production photocatalyst. *Appl. Catal. B* **2019**, *243*, 556-565. DOI: 10.1016/j.apcatb.2018.11.011

[21] Zhang, L.; Zhang, J.; Yu, H.; Yu, J. Emerging S-Scheme Photocatalyst. *Adv. Mater.* **2022**, *34*, 2107668. DOI: 10.1002/adma.202107668

[22] Bao, Y.; Song, S.; Yao, G.; Jiang, S. S-Scheme Photocatalytic Systems. *Sol. RRL* **2021**, *5*, 2100118. DOI: 10.1002/solr.202100118

[23] Wang, L.; Sun, J.; Cheng, B.; He, R.; Yu, J. S-Scheme Heterojunction Photocatalysts for H_2O_2 Production. *J. Phys. Chem. Lett.* **2023**, *14*, 4803-4814. DOI: 10.1021/acs.jpclett.3c00811

[24] Kumar, P.; Laishram, D.; Sharma, R. K.; Vinu, A.; Hu, J.; Kibria, M. G. Boosting Photocatalytic Activity Using Carbon Nitride Based 2D/2D van der Waals Heterojunctions *Chem. Mater.* **2021**, *33*, 9012-9092. DOI: 10.1021/acs.chemmater.1c03166

[25] Zhang, Y.; Shen, G.; Sheng, C.; Zhang, F.; Fan, W. The effect of piezo-photocatalysis on enhancing the charge carrier separation in $BaTiO_3/KNbO_3$ heterostructure photocatalyst. *Appl. Surf. Sci.* **2021**, *562*, 150164. DOI: 10.1016/j.apsusc.2021.150164

[26] Jing, L.; Xu, Y.; Xie, M.; Li, Z.; Wu, C.; Zhao, H.; Wang, J.; Wang, H.; Yan, Y.; Zhong, N.; Li, H.; Hu, J. Piezo-photocatalysts in the field of energy and environment: Designs, applications, and prospects. *Nano Energy* **2023**, *112*, 108508. DOI: 10.1016/j.nanoen.2023.108508

[27] Wei, H.; Meng, F.; Zhang, H.; Yu, W.; Li, J.; Yao, S. Novel oxygen vacancy-rich Bi_2MoO_6-SOVs/$MgFe_2O_4$ S-scheme heterojunction piezo-photocatalytic for efficient degradation of norfloxacin and theoretical calculations. *Chem. Eng. J.* **2024**, *479*, 147738. DOI: 10.1016/j.cej.2023.147738

[28] Preeyanghaa, M.; Vinesh, V.; Neppolian, B.; Construction of S-scheme 1D/2D rod-like g-C_3N_4/V_2O_5 heterostructure with enhanced sonophotocatalytic degradation for Tetracycline antibiotics. *Chemosphere* **2022**, *287*, 132380. DOI: 10.1016/j.chemosphere.2021.132380

[29] Jang, W. Y.; Reddy, C. V.; Daouli, A.; Kakarla, R. R.; Bandaru, N.; Shim, J.; Badawi, M.; Aminabhavi, T. M. Novel 2D sulfur-doped V_2O_5 flakes and their applications in photoelectrochemical water oxidation and high-performance energy storage supercapacitors. *Chem. Eng. J.* **2023**, *461*, 141935. DOI: 10.1016/j.cej.2023.141935

[30] Tran, D. D.; Vuong, H.-T.; Nguyen, D.-V.; Ly, P. P.; Phan, P. D. M.; Khoi, V. H.; Mai, P. T.; Hieu, N. H. Revisiting the roles of dopants in g-C_3N_4 nanostructures for piezo-photocatalytic production of H_2O_2: a case study of selenium and sulfur. *Nanoscale Adv.* **2023**, *5*, 2327. DOI: 10.1039/D2NA00909A

[31] Dang, T. T.; Nguyen, T. K. A.; Bhamu, K. C.; Mahvelati-Shamsabadi, T.; Van, V. K. H.; Shin, E. W.; Chung, K.-H.; Hur, S. H.; Choi, W. M.; Kang, S. G.; Chung, J. S. Engineering Holey Defects on 2D Graphitic Carbon Nitride Nanosheets by Solvolysis in Organic Solvents. *ACS Catal.* **2022**, *12*, 13763−13780. DOI: 10.1021/acscatal.2c03523

[32] Vuong, H.-T.; Mahvelati-Shamsabadi, T.; Dang, T. T.; Dao, Q. D.; Shin, E. W.; Chung, J. S. Bandgap control of p-n heterojunction of Cu-Cu_2O@ZnO with modified reduced graphene oxide nanocomposites for photocatalytic hydrogen evolution. *Int. J. Hydrog. Energy* **2022**, *47*, 23249-23263. DOI: 10.1016/j.ijhydene.2022.05.139

[33] Parida, M. R.; Vijayan, C.; Rout, C. S.; Sandeep, C. S. S.; Philip, R.; Deshmukh, P. C. Room Temperature Ferromagnetism and Optical Limiting in V_2O_5 Nanoflowers Synthesized by a Novel Method. *J. Phys. Chem. C* **2011**, *115*, 112-117. DOI: 10.1021/jp107862n

[34] Yuan, Y.; Zhang, L.; Xing, J.; Utama, M. I. B.; Lu, X.; Du, K.; Li, Yo.; Hu, X.; Wang, S.; Genç, A.; Dunin-Borkowski, R.; Arbiol, J.; Xiong, Q. High-yield synthesis and optical properties of g-C3N4. *Nanoscale* **2015**, *7*, 12343. DOI: 10.1039/C5NR02905H

[35] Yu, H.; Shi, R.; Zhao, Y.; Bian, T.; Zhao, Y.; Zhou, C.; Waterhouse, G. I. N.; Wu, L.-Z.; Tung, C.-H.; Zhang, T. Alkali-Assisted Synthesis of Nitrogen Deficient Graphitic Carbon Nitride with Tunable Band Structures for Efficient Visible-Light-Driven Hydrogen Evolution. *Adv. Mater.* **2017**, *29*, 1605148. DOI: 10.1002/adma.201605148

[36] Shiraishi, Y.; Kofuji, Y.; Sakamoto, H.; Tanaka, S.; Ichikawa, S.; Hirai, T. Effects of Surface Defects on Photocatalytic H_2O_2 Production by Mesoporous Graphitic Carbon Nitride under Visible Light Irradiation. *ACS Catal.* **2015**, *5*, 3058-3066. DOI: 10.1021/acscatal.5b00408

[37] Phan, P. D. M.; Nguyen, D.-V.; Anh, N. H.; Toan, H. P.; Ly, P. P.; Bui, D.-P.; S. H. Hur, Ung, T. D. T.; Bich, D. D.; Vuong, H.-T. S-Scheme Heterostructured CdS/g-C_3N_4

Nanocatalysts for Piezo-Photocatalytic Synthesis of H_2O_2. *ACS Appl. Nano Mater.* **2023**, *6*, 16702-16715. DOI: 10.1021/acsanm.3c02933

[38] Ge, H.; Xu, F.; Cheng, B.; Yu, J.; Ho, W. S-Scheme Heterojunction TiO2/CdS Nanocomposite Nanofiber as H_2-Production Photocatalyst. *ChemCatChem* **2019**, *11*, 6301-6309. DOI: 10.1002/cctc.201901486

[39] Xu, F.; Meng, K.; Cheng, B.; Wang, S.; Xu, J.; Yu, J. Unique S-scheme heterojunctions in self-assembled TiO_2/$CsPbBr_3$ hybrids for CO_2 photoreduction. *Nat. Commun.* **2020**, *11*, 4613. DOI: 10.1038/s41467-020-18350-7

[40] Bai, J.; Chen, W.; Hao, L.; Shen, R.; Zhang, P.; Li, N.; Li, X. Assembling Ti_3C_2 MXene into $ZnIn_2S_4$-$NiSe_2$ S-scheme heterojunction with multiple charge transfer channels for accelerated photocatalytic H_2 generation. *Chem. Eng. J.* **2022**, *447*, 137488. DOI: 10.1016/j.cej.2022.137488

[41] Sangamithirai, D.; Ramanathan, S. Electrochemical sensing platform for the detection of nitroaromatics using g-C_3N_4/V_2O_5 nanocomposites modified glassy carbon electrode. *Electrochimica Acta* **2022**, *434*, 141308. DOI: 10.1016/j.electacta.2022.141308

[42] Wang, S.; Song, Y.; Ma, Y.; Zhu, Z.; Zhao, C.; Zhao, C. Attaining a high energy density of 106 Wh kg^{-1} for aqueous supercapacitor based on VS_4/rGO/CoS_2@Co electrode. *Chem. Eng. J.* **2019**, *365*, 88-98. DOI: 10.1016/j.cej.2019.02.031

[43] Zhang, J.; Li, Z.; Liu, B.; Chen, M.; Zhou, Y.; Zhu, M. Insights into the role of C-S-C bond in C_3N_5 for photocatalytic NO deep oxidation: Experimental and DFT exploration. *Appl. Catal. B* **2023**, *328*, 122522. DOI: 10.1016/j.apcatb.2023.122522

[44] Li, Q.; Guo, B.; Yu, J.; Ran, J.; Zhang, B.; Yan, H.; Gong, J. R.; Highly Efficient Visible-Light-Driven Photocatalytic Hydrogen Production of CdS-Cluster-Decorated Graphene Nanosheets. *J. Am. Chem. Soc.* **2011**, *133*, 10878-10884. DOI: 10.1021/ja2025454

[45] Vuong, H.-T.; Nguyen, D.-V.; Ly, P. P.; Phan, P. D. M.; Nguyen, T. D.; Tran, D. D.; Mai, P. T.; Hieu, N. H. Defect Engineering of Porous g-C_3N_4 to Add Multifunctional Groups for Enhanced Production of H_2O_2 via Piezo-Photocatalysis. *ACS Appl. Nano Mater.* **2023**, *6*, 664-676. DOI: 10.1021/acsanm.2c04829

[46] Vuong, H.-T.; Bui, D.-P.; Nguyen, D.-V.; Phuong, L. P.; Minh, P. P. D.; Dat, T. D.; Hieu, N. H. Graphitic Carbon Nitride Based Materials Towards Photoproduction of H_2O_2. *ChemPhotoChem* **2023**, *7*, e202200299. DOI: 10.1002/cptc.202200299

[47] Ly, P. P.; Nguyen, D.-V.; Luu, T. A.; Hung, N. Q.; Hue, P. T.; Hue, N. T. N.; Pham, M.-T.; Ung, T. D. T.; Bich, D. D.; Phan, P. D. M.; Anh, N. H.; Toan, H. P.; Bui, D.-P.; Dao,V.-A.; Hur, S. H.; Vuong, H.-T. Insights into Molten Salts Induced Structural Defects in Graphitic Carbon Nitrides for Piezo-Photocatalysis with Multiple H_2O_2 Production Channels. *Adv. Sustainable Syst.* **2023**, 2300470. DOI: 10.1002/adsu.202300470

[48] Fu, C.; Mengyu Zhao, Xuan Chen, Guowei Sun, Chan Wang, Qijun Song. Unraveling the dual defect effects in C_3N_5 for piezo-photocatalytic degradation and H_2O_2 generation. *Appl. Catal. B* **2023**, *332*, 122752. DOI: 10.1016/j.apcatb.2023.122752

[49] Bao, N.; Hu, X.; Zhang, Q.; Miao, X.; Jie, X.; Zhou, S. Synthesis of porous carbon-doped g-C_3N_4 nanosheets with enhanced visible-light photocatalytic activity. *Appl. Surf. Sci.* **2017**, *403*, 682-690. DOI: 10.1016/j.apsusc.2017.01.256

[50] Palanisamy, G.; Bhuvaneswari, K.; Srinivasan, M.; Vignesh, S.; Elavarasan, N.; Venkatesh, G.; Pazhanivel, T.; Ramasamy, P. Two-dimensional g-C_3N_4 nanosheets supporting Co_3O_4-V_2O_5 nanocomposite for remarkable photodegradation of mixed organic dyes based on a dual Z-scheme photocatalytic system. *Diam. Relat. Mater.* **2021**, *118*, 108540. DOI: 10.1016/j.diamond.2021.108540

[51] Fauzi, M.; Esmaeilzadeh, F.; Mowla, D.; Sahraeian, N. The effect of various capping agents on V_2O_5 morphology and photocatalytic degradation of dye. *J Mater Sci: Mater Electron* **2021**, *32*, 10473–10490. DOI: 10.1007/s10854-021-05703-1

[52] Patel, S. B.; Vasava, D. V. Synthesis and Characterization of Ag@g−C_3N_4 and Its Photocatalytic Evolution in Visible Light Driven Synthesis Of Ynone. *ChemCatChem* **2020**, *12*, 631-641. DOI: 10.1002/cctc.201901802

[53] Tang, J.-Y.; Kong, X. Y.; Ng, B.-J.; Chew, Y.-H.; Mohamed, A. R.; Chai, S.-P. Midgap-state-mediated two-step photoexcitation in nitrogen defect-modified g-C3N4 atomic layers for superior photocatalytic CO_2 reduction. *Catal. Sci. Technol.* **2019**, *9*, 2335. DOI: 10.1039/C9CY00449A

[54] Sun, D.; Li, L.; Yu, Y.; Huang, L.; Meng, F.; Su, Q.; Ma, S.; Xu, B. B and cyano groups co-doped g-C_3N_4 with multiple defects for photocatalytic nitrogen fixation in ultrapure water without hole scavengers. *J. Colloid. Interface Sci.* **2021**, *600*, 639-648. DOI: 10.1016/j.jcis.2021.05.075

[55] Bui, D.-P.; Pham, M.-T.; Tran, H.-H.; Nguyen, T.-D.; Cao, T. M.; Pham, V. V.; Revisiting the Key Optical and Electrical Characteristics in Reporting the Photocatalysis of Semiconductors. *ACS Omega* **2021**, *6*, 27379-27386. DOI: 10.1021/acsomega.1c04215

[56] Huang, H.; Liu, K.; Chen, K.; Zhang, Y.; Zhang, Y.; Wang, S. Ce and F Comodification on the Crystal Structure and Enhanced Photocatalytic Activity of Bi_2WO_6 Photocatalyst under Visible Light Irradiation. *J. Phys. Chem. C* **2014**, *118*, 14379-14387. DOI: 10.1021/jp503025b

[57] Shi, J.; Cui, H.; Liang, Z.; Lu, X.; Tong, Y.; Su, C.; Liu, H. The roles of defect states in photoelectric and photocatalytic processes for $Zn_xCd_{1-x}S$. *Energy Environ. Sci.* **2011**, *4*, 466-470. DOI: 10.1039/C0EE00309C

[58] Zhu, Y.; Ling, Q.; Liu¸ Y.; Wang, H.; Zhu, Y. Photocatalytic performance of $BiPO_4$ nanorods adjusted via defects. *Appl. Catal. B* **2016**, *187*, 204-211. DOI:

[59] Rouby, W. M. A. E.; Aboubakr, A. E. A.; Khan, M. D.; Farghali, A. A.; Millet, P.; Revaprasadu, N. Synthesis and characterization of Bi-doped g-C3N4 for photoelectrochemical water oxidation. *Sol. Energy* **2020**, *211*, 478-487. DOI: 10.1016/j.apcatb.2016.01.012

[60] Liang, C.; Niu, H.-Y.; Guo, H.; Niu, C.-G.; Huang, D.-W.; Yang, Y.-Y.; Liu, H.-Y.; Shao, B.-B.; Feng, H.-P. Insight into photocatalytic nitrogen fixation on graphitic carbon nitride: Defect-dopant strategy of nitrogen defect and boron dopant. *Chem. Eng. J.* **2020**, *396*, 125395. DOI: 10.1016/j.cej.2020.125395

[61] Eroglu, Z.; Metin, O. Internal Interactions within the Complex Type-II Heterojunction of a Graphitic Carbon Nitride/Black Phosphorus Hybrid Decorated with Graphene Quantum Dots: Implications for Photooxidation Performance. *ACS Appl. Nano Mater.* **2023**, *6*, 7960-7974. DOI: 10.1021/acsanm.3c01187

[62] Zhang, X.; Zha, X.; Luo, Y.; Liu, T.; Chen, G.; He, X. In_2O_3 Nanoparticle/$Bi_4O_5Br_2$ Nanosheet S-Scheme Heterojunctions with Interfacial Oxygen Vacancies for Photocatalytic Degradation of Tetracycline. *ACS Appl. Nano Mater.* **2023**, *6*, 11877-11887. DOI: 10.1021/acsanm.3c01720

[63] Vuong, H.-T.; Mahvelati-Shamsabadi, T.; Dang, T. T.; Hur, S. H.; Chung, J. S. EDTA Linker for S-scheme CdS/Spinel Oxides Heterojunction Photocatalyst for Visible-Light-Driven Hydrogen Production. *Korean J. Chem. Eng.* **2024**, *41*, 309-323. DOI: 10.1007/s11814-024-00087-4